COMMUNICATION

Check for updates

Capping agent optimization of high entropy alloy nanoparticles enhances electrocatalytic water splitting

Sangmin Jeong, [ID] Silas W. Bollen, [ID] Porvajja Nagarajan [ID] and Michael B. Ross [ID] *

By leveraging a capping-agent assisted approach, ultrasmall and highly dispersed AuPdRuRhPt high entropy alloy (HEA) nanoparticles are synthesized, overcoming aggregation challenges and enabling control over atomic-scale mixing and coordination environments among the constituent metals. Using polyethylene glycol (PEG) and polyvinylpyrrolidone (PVP) as capping agents, we obtained uniform nanoparticles (<10 nm) with improved catalytic stability and active site accessibility. Structural characterization using high-resolution transmission electron microscopy (HR-TEM), synchrotron wide-angle X-ray scattering (WAXS), pair distribution function (PDF) analysis, and X-ray photoelectron spectroscopy (XPS) revealed that the capping agent influences the size and the atomic arrangement of the HEA structure, which is crucial for optimizing catalytic activity. PEG-capped HEA NPs exhibited superior catalytic activity for both the HER (122 mV@-0.01 mA cm^{-2} ECSA) and the OER (220 mV@-0.01 mA cm^{-2} ECSA), with lower overpotentials compared to Pt/C and IrO$_2$. These results emphasize the critical role of capping agents in optimizing both the electrochemical performance and stability of HEA nanoparticles, offering valuable insights for the design of efficient electrocatalysts for energy conversion applications.

New concepts

We demonstrate a unique capping-agent-assisted synthesis strategy for noble metal high entropy alloy (HEA) nanoparticles, effectively overcoming aggregation issues while optimizing metal–metal interactions. By incorporating polyethylene glycol (PEG) or polyvinylpyrrolidone (PVP), we obtained ultrasmall and uniformly distributed HEA nanoparticles (<10 nm), significantly enhancing catalytic stability and active site accessibility. Unlike conventional HEA synthesis, which often leads to particle agglomeration and inconsistent catalytic performance, our approach ensures well-dispersed nanoparticles with prolonged active site exposure. The capped HEA NPs exhibited exceptional electrocatalytic performance, achieving an onset potential of 122 mV for the hydrogen evolution reaction (HER) and 220 mV for the oxygen evolution reaction (OER) in 0.5 M H$_2$SO$_4$. Notably, after normalizing with electrochemical surface area (ECSA), the catalysts outperformed commercial Pt/C (160 mV@-0.01 mA cm^{-2} ECSA) and IrO$_2$ (330 mV@0.01 mA cm^{-2} ECSA). This study presents a new strategy for synthesizing HEA nanoparticles, showing that capping agents stabilize the structure while enhancing intrinsic catalytic activity through electronic and interfacial optimization. These insights advance the design of efficient, durable HEA-based electrocatalysts for energy conversion.

Department of Chemistry, University of Massachusetts Lowell, Lowell, MA 01854, USA.
E-mail: michael_ross@uml.edu

Congratulations to ten impactful years of sharing innovative nanoscience! It is a great honour to serve on the Community Board for Nanoscale Horizons. We are excited to contribute this work showing how nanoscale design and advanced X-ray science can together advance societal challenges in energy and materials innovation. We look forward to continuing to be a part of Nanoscale Horizons' bright future.

Michael B. Ross

Introduction

The pivot towards renewable energy sources has accelerated efforts in efficient hydrogen production through water-splitting reactions, establishing it as one of the key technologies that enables the generation of CO$_2$ emission-free fuel sources.[1,2] Electrocatalysts for the hydrogen evolution reaction (HER) and oxygen evolution reaction (OER) play a crucial role in determining the efficiency and viability of hydrogen production.[3–5] The sluggish kinetics of water-splitting reactions, specifically the OER, which involves a complex four-electron process, poses a persistent challenge in achieving an efficient electrocatalytic system.[6–8] The existing large-scale systems predominantly use monometallic platinum group metal (PGM) catalysts, such as platinum, iridium, and ruthenium, which are known for their

remarkable performance but have limitations in catalytic efficiency due to challenges in optimizing binding energies for multiple reaction intermediates.[9] Additionally, higher loading requirements of PGM elements compromise economic viability and deter widespread implementation. Therefore, there is a critical scientific need to develop electrocatalysts with enhanced activity while reducing precious metal content.

Electrocatalysts that act as bifunctional catalysts are highly desirable for efficient water-splitting reactions due to their multiple active sites and synergistic effects.[10] High entropy alloys (HEAs) are a class of materials typically composed of five or more principal elements, in equal or near-equimolar concentrations, maximizing the disorder or randomness at the atomic level.[11-13] This high configurational entropy (ΔS_{config}) effectively reduces the Gibbs free energy ($\Delta G = \Delta H - T\Delta S$) of the alloy system, thereby promoting thermodynamic stability even among elements with substantial atomic size and electronegativity differences.[14,15] These HEAs, when reduced to the nanoscale, exhibit a high density of surface-active atoms, which enhances their performance in electrocatalytic water splitting reactions, including the HER and OER.[16] However, ultrasmall HEA nanoparticles are prone to agglomeration during synthesis, which limits their catalytic performance by reducing accessible surface area.[17] To harness the size-dependent catalytic advantages, a deliberate strategy is required to prevent aggregation and ensure uniform dispersion.

Here, we explore capping-agent-mediated HEA design to address aggregation[18] and the feasibility of ultrasmall HEA nanoparticles for electrochemical applications by integration of polyethylene glycol (PEG) or polyvinylpyrrolidone (PVP).[19,20] PEG and PVP have been extensively employed for controlling the size of single-metal nanoparticles (e.g. Au,[21,22] Ag,[23] and Fe[24]), with numerous studies underscoring their notable stabilization capability. More recently, these capping agents have also been extended to HEA synthesis.[25,26] However, their use in HEA synthesis has been associated with potential challenges, such as the blockage of catalytic active sites,[27] uneven alloy composition,[28] and thermal instability.[27,29] We report a controlled, facile synthesis of PVP- and PEG-capped AuPdRuRhPt HEA nanoparticles on carbon supports via a wet-chemical approach.[30] The noble metals Pd, Ru, Rh, and Pt were chosen due to their inherent bifunctionality for HER and OER processes, as well as their optimum proton and hydroxide adsorption energies.[31] Unlike previous methods, our room-temperature NaBH$_4$–HCl reduction with minimal PEG (250 μM) and PVP (1.25 mM) produces stabilized HEA nanoparticles free from site blockage and thermal instability. The as-synthesized PEG-capped HEA nanoparticles have a uniform diameter of 1.9 ± 0.49 nm. In 0.5 M H$_2$SO$_4$ electrolyte, they displayed an overpotential of 87 mV for the HER and 270 mV for the OER, with HER current density increasing by 2.48% (from 161 mA cm^{-2} to 165 mA cm^{-2}) and OER overpotential slightly increasing by 1.96% (from 1.53 V to 1.56 V) over a 24-hour period, demonstrating robust catalytic performance with minimal degradation. This work examines the synthesis and characterization of PGM-based HEAs, with particular emphasis on the influence of

capping agents, such as PEG and PVP, on the physicochemical properties and catalytic behavior in HER and OER processes.[32]

Experimental

Nanoparticle synthesis

PVP- and PEG-capped AuPdRuRhPt HEA nanoparticles were synthesized from Au, Pd, Ru, Rh and Pt precursor salts via a wet-chemical process. The precursors were prepared by dissolving 2.5 mmol of HAuCl$_4$ (99.99% metals basis, Thermo Scientific), 2.5 mmol of K$_2$PdCl$_4$ (99.99% metals basis, Alfa Aesar), 2.5 mmol of RuCl$_3$ (99.99% metals basis, Thermo Scientific), 2.5 mmol of RhCl$_3$ (99.99% metals basis, Alfa Aesar), and 2.5 mmol of PtCl$_4$ (99.99% metals basis, Alfa Aesar) in ultrapure water. Additional stock solutions of 1.25 mM poly(N-vinyl-2-pyrrolidone) (PVP, M.W. 40 000 g mol^{-1}, Alfa Aesar), 250 μM polyethylene glycol (PEG, M.W. 8000 g mol^{-1}, Alfa Aesar), 0.5 wt% carbon black (XC-72, Fuel Cell Earth), and 5 M hydrochloric acid (HCl, Fisher Chemical) were prepared using ultrapure water. For the synthesis, a 20 mL glass vial with a stir bar containing ultrapure water (total volume of 5 mL) was stirred at 1500 rpm. Depending on the capping agent, either 50 μL of PEG or 100 μL of PVP stock solution was added, followed by 100 μL of carbon black solution, 200 μL of each metal precursor, and 100 μL of 5 M HCl. A freshly prepared 1 M sodium borohydride (NaBH$_4$, 97%, Alfa Aesar) solution (100 μL) was then introduced. The product was briefly sonicated, transferred to microcentrifuge tubes, and centrifuged at 21 300 rcf for 25 minutes. After discarding the supernatant, the pellet was resuspended in ultrapure water, sonicated, and combined. The washing and centrifugation process was repeated 1–2 times before collecting the final purified nanoparticles for further characterization.

Characterization of materials

The morphology and structural analyses were performed on a high-resolution scanning transmission electron microscope (HR-STEM, JEOL, JEM-2100 Plus, 200 kV) and a conventional TEM (Philips CM12). Energy dispersive X-ray spectroscopy (EDS) with elemental mapping was conducted using a JEM-2100 Plus. The crystal phase and structure were characterized by X-ray diffraction (XRD) using a Rigaku Miniflex X-ray diffractometer (CuKα, λ = 1.5406 Å). Synchrotron wide-angle X-ray scattering (WAXS) and X-ray pair distribution function (PDF) measurements were also performed. All synchrotron X-ray experiments were conducted at beamline 28-ID-1 at the NSLS-II, Brookhaven National Laboratory using a high-energy X-ray source (λ = 0.1665 Å) to enhance resolution. To ensure accuracy, the LaB$_6$ standard was employed to calibrate both the sample-to-detector distance and the beam center positions. The PDF simulation model was generated by obtaining chemical bonding data from the open-source Materials Project database,[33] and this information was used to regenerate the local structure of the bimetallic alloys using PDFgui[34] (Fig. S3). X-ray photoelectron spectroscopy (XPS) was performed on a K-Alpha spectrometer (Thermo Fisher Scientific, K-Alpha, USA) with a monochromatic Al Kα radiation

source, and HR-XPS peaks were calibrated to the C 1s peak at 284.8 eV. Elemental analysis was conducted by total reflection X-ray fluorescence (TXRF) using a Bruker S2 Picofox equipped with a molybdenum source; the samples were prepared by drop-casting 10 µL of the washed product onto quartz discs, air-dried for 1 hour, and analyzed over the 0–17.5 keV range for 1000 s using a standardless method. Thermogravimetric analysis (TGA) was performed using a TA Instruments Q50 analyzer at a heating rate of 10 °C min^{-1} under a nitrogen atmosphere.

Electrochemical water-splitting measurements

All electrochemical measurements were performed at ambient temperature ($\sim$25 °C) using an electrochemical potentiostat (Pine Research, WaveDriver 100) connected to a commercial three-electrode system in an acidic electrolyte, 0.5 M H$_2$SO$_4$. A Pt mesh and a silver/silver chloride electrode (Ag/AgCl) were used as the counter and reference electrodes, respectively. For the preparation of the working electrode, an electrocatalyst ink was prepared by sonicating a solution mixture containing 1 mg of PVP- and PEG-capped AuPdRuRhPt HEA nanoparticles with 3 mg of vulcanized carbon black, 50 µL Nafion (5 wt%, Thermo Scientific), and 300 µL isopropyl alcohol (IPA, Ricca) for 1 h. Then, 10 µL of the ink solution was drop-cast onto a glassy carbon electrode (active area of 0.07 cm^2). To benchmark the HER and OER activity, commercial Pt/C (10%, Thermo Scientific) and IrO$_2$ (99.99% metals basis, Alfa Aesar) were prepared and evaluated separately. All the potentials *vs.* Ag/AgCl reference values were converted to the reversible hydrogen electrode (RHE) using the Nernst equation as follows:

$$E_{RHE} = E_{Ag/AgCl} + (0.0591 \times pH) + E^0_{Ag/AgCl}$$

where E_{RHE} is the converted potential *vs.* the reference electrode, $E_{Ag/AgCl}$ is the experimentally measured potential, and $E^0_{Ag/AgCl}$ is the standard potential of Ag/AgCl (0.197 V at 25 °C). The HER and OER activity of PVP- and PEG-capped AuPdRuRhPt HEA nanoparticles was evaluated by linear sweep voltammetry (LSV), Tafel slope analysis, cyclic voltammetry (CV), double layer capacitance (C_{dl}), and electrochemical impedance spectroscopy (EIS) in 0.5 M H$_2$SO$_4$ electrolyte, with a Pt mesh as the counter electrode. LSV data were measured in the range of -0.5 V to 0.1 V *vs.* RHE at a rate of 5 mV s^{-1} and converted to the Tafel slope using raw data after performing

LSV. CV data were measured in each potential range based on the electrolyte at various scan rates (10–80 mV s^{-1}). The C_{dl} of the catalysts was calculated from CV using the equation:

$$C_{dl} = \frac{\Delta j(j_a - j_c)}{2\nu}$$

where j_a and j_c are the anodic and cathodic current densities, respectively, and ν is the scan rate in mV s^{-1} from CV. EIS measurements were performed using a Nyquist plot in the range of 100 kHz to 0.1 Hz at 10 mA cm^{-2}. Chronoamperometry measurements were conducted at sample-specific potentials (-0.40 to -0.41 V *vs.* Ag/AgCl) to achieve current densities above 100 mA cm^{-2}, enabling a direct comparison of catalytic performance across samples. The TOF of the catalysts was determined using the following equation:

$$TOF\ (s^{-1}) = I/nFN_S$$

$$TOF\ (s^{-1})_{ECSA} = I/nFN_S^{ECSA}$$

where I is the measured current (mA), F is the Faraday constant (96 485 C mol^{-1}), n is the number of electrons transferred per molecule of product (2 for the HER), N_S is the number of activities (mol) and N_S^{ECSA} is the number of electrochemically active sites determined from ECSA (mol cm^{-2}). In contrast, OER stability tests were performed using chronopotentiometry at a fixed current density of 10 mA cm^{-2}. The experimental data were fitted using Pine-view software and Origin software using appropriate equivalent circuits.

Results and discussion

The synthesis of HEA nanoparticles often requires high-temperature and high-pressure environments to form a stable, ultrasmall, high entropy state.[35,36] Our work implements a simple, straightforward wet-chemical synthesis where all the different metal precursors are reduced using NaBH$_4$ in a vial with the desired capping agent (PEG and PVP), an acid as the shape directing agent (HCl), and a supporting material (vulcanized carbon) (schematics in Fig. 1; see details in the Experimental section). The capping agents PEG and PVP facilitate stabilization by binding to the nanoparticle surface through their carbonyl or lactam groups preventing aggregation
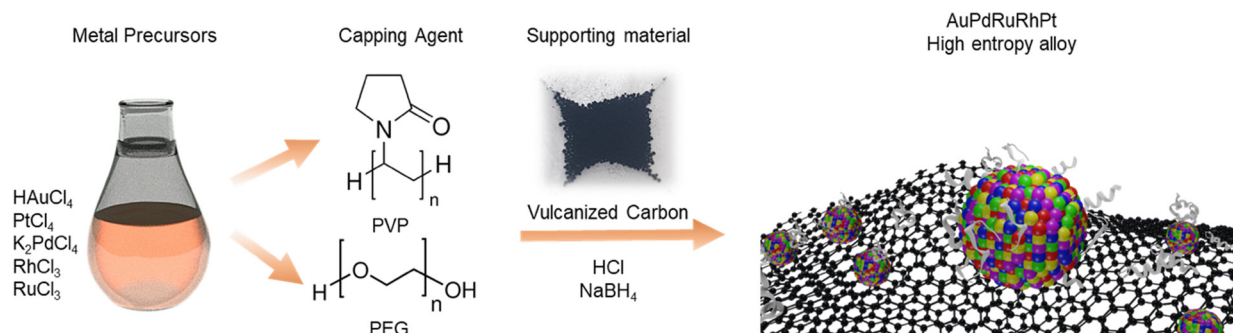

Fig. 1 Schematics of the wet-chemical synthesis of capped AuPdRuRhPt HEA nanoparticles.

through steric hindrance, which further aids in controlling the particle size and shape during synthesis.[19,20]

The PEG- and PVP-capped AuPdRuRhPt HEA nanoparticles were characterized using high-resolution scanning transmission electron microscopy (HR-STEM) along with elemental mapping and X-ray diffraction techniques. HR-TEM analysis confirmed the successful synthesis of carbon-supported ultrasmall nanoparticles with distinctive spherical features (Fig. 2 and 3). The nanoparticles exhibited small diameters with an average values of 1.98 nm for PEG-capped HEA NPs (Fig. S1) and 6.5 nm for PVP-capped ones (Fig. S2). This size disparity likely stems from the distinct stabilization mechanisms of each capping agent. PVP is known to be a strong capping agent that effectively controls particle growth and maintains structural integrity during synthesis and subsequent electrochemical processes.[37] In contrast, PEG appears to limit growth more significantly, resulting in the formation of much smaller nanoparticles. These observations highlight the role of capping agents in achieving ultrasmall nanoparticles compared to the previously reported HEA nanoparticle systems.[30]

To further investigate the role of capping agents, AuPdRuRhPt HEA nanoparticles were also synthesized without any PEG or PVP. HR-TEM analysis showed significantly larger nanoparticles with a broad size distribution of 3–40 nm (Fig. S3). These observations clearly demonstrate that both PEG and PVP are essential for controlling particle size and achieving uniform morphology in HEA nanoparticle synthesis.

Atomic-level structural investigation through high-magnification imaging identified interplanar spacings of 2.12 Å and 2.17 Å for PEG- and PVP-capped AuPdRuRhPt HEA nanoparticles, respectively. These measurements, attributable to the (111) crystallographic planes, were verified through fast Fourier transform analysis (inset of Fig. 2b and 3b). Crystallographic analysis using synchrotron WAXS revealed distinct long-range diffraction peaks corresponding to the (111), (200), and (220) facets in both HEA nanoparticle variants (Fig. 2c and 3c), confirming their face-centered cubic crystalline structure. Although the PEG-capped AuPdRuRhPt HEA nanoparticles exhibited slightly stronger diffraction peaks, the PVP-capped ones also showed high crystallinity by WAXS, suggesting that both capping agents contribute effectively to the overall structural quality.

The smaller size and greater uniformity of the PEG-capped AuPdRuRhPt HEA nanoparticles are likely responsible for their enhanced electrochemical performance, as they expose more active sites and facilitate more efficient charge transfer during catalytic reactions.[38–40] While both PEG and PVP show pronounced crystallinity in WAXS, the PVP-capped AuPdRuRhPt HEA nanoparticles also exhibit high-quality diffraction patterns, with clear long-range ordering in the (111), (200), and (220) peaks, indicating a well-developed crystalline structure. TEM and PDF analyses confirm these structural insights, revealing consistent atomic spacing and demonstrating that particle size distribution and crystallographic ordering play a
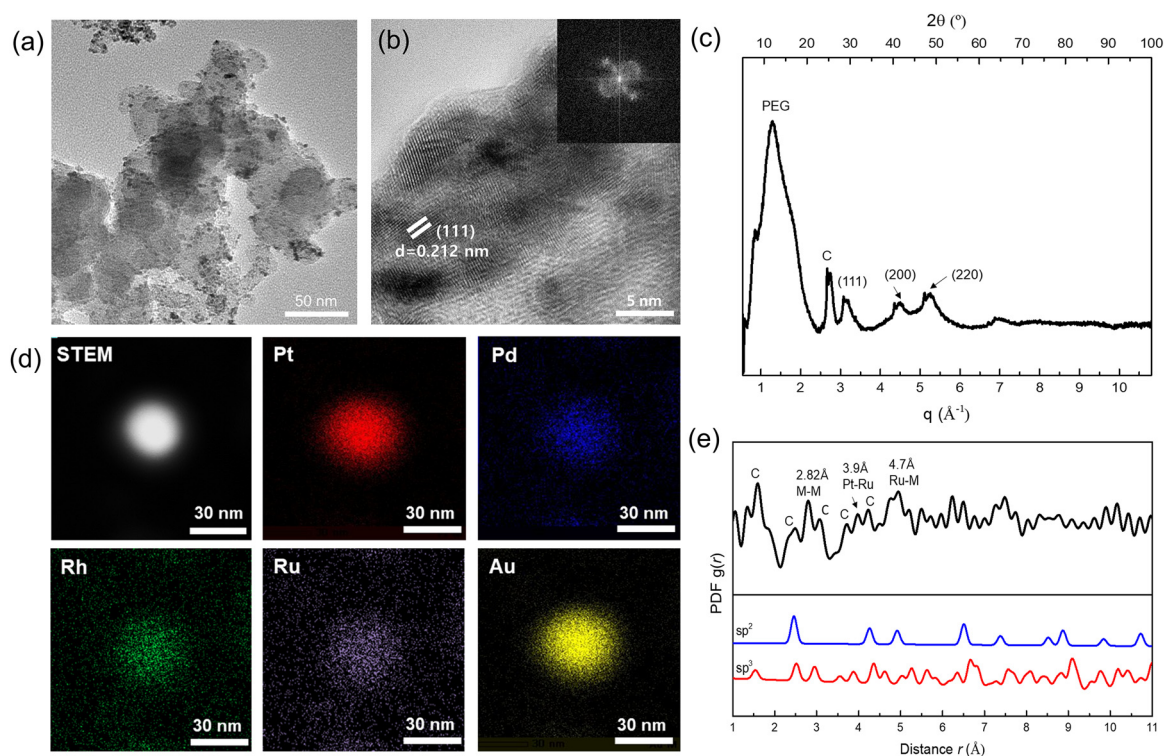
Fig. 2 Characterization of the structure and crystallinity of PEG–capped HEA NPs. (a) and (b) HR-TEM images showing the morphology of a nanoparticle with (111) d-spacing, (c) synchrotron wide-angle X-ray scattering (WAXS) pattern showing the crystallinity of PEG-capped HEA NPs, (d) STEM−EDS mapping results displaying the elemental maps of Pt, Pd, Rh, Ru, and Au, and (e) synchrotron X-ray pair distribution function (PDF) results revealing local structure characterization with experimental and simulated PDF data (inset: carbon model; sp^2: blue, sp^3: red).
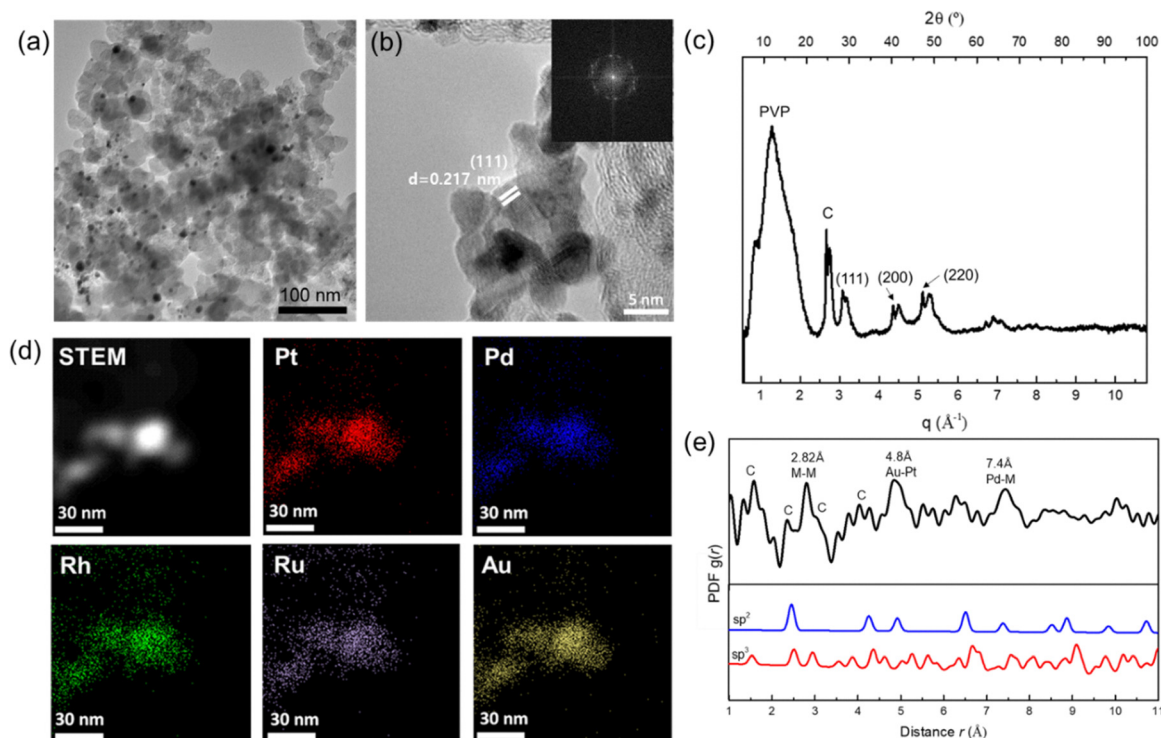
Fig. 3 Characterization of the structure and crystallinity of PVP-capped HEA NPs. (a) and (b) HR-TEM images showing the morphology of a nanoparticle with (111) *d*-spacing, (c) synchrotron WAXS pattern showing the crystallinity of PVP-capped HEA NPs, (d) STEM–EDS mapping results displaying the elemental maps of Pt, Pd, Rh, Ru, and Au, and (e) synchrotron PDF results revealing local structure characterization with experimental and simulated PDF data (inset: carbon model; sp^2: blue, sp^3: red).

key role in achieving enhanced electrochemical performance. The elemental distribution of Pt, Pd, Rh, Ru, and Au obtained from the STEM–EDS mapping demonstrated homogeneous spatial distribution of all five constituent elements within individual nanoparticles, with no detectable segregation (Fig. 2d and 3d). In the absence of capping agents, STEM–EDS mapping of AuPd-RuRhPt nanoparticles showed inhomogeneous distribution of Pt, Pd, Rh, Ru, and Au across the nanoparticles (Fig. S4). This uniform elemental distribution observed in the capped nanoparticles is essential for controlling catalytic activity and stability during prolonged electrochemical operation. To preserve nanostructure integrity during the analysis, larger particles were selected for mapping procedures, and electron beam exposure was methodically limited to under 10 minutes to prevent beam-induced alterations to the specimens.

Fig. 2e and 3e present the crucial elemental characteristics of both variants and their crystallographic fingerprints at the atomic level. The PDF plots of both variants show a peak at 2.82 Å corresponding to metal–metal (M–M) bonds (Fig. S5) with the subsequent peaks revealing important differences in atomic arrangements. The plots indicate several distinguishing peaks: 3.9 Å (Pt–Ru) and 4.7 Å (Ru–M) for the PEG-capped system, and 4.8 Å and 7.4 Å (Pd–M) for the PVP-capped system, suggesting that there are different preferential atomic arrangements. This establishes the relationship between interatomic distances and the overall structural arrangement. These distinct diffraction features suggest that the capping agent influences not only the

overall size but also the atomic arrangement within the HEA structure. Furthermore, the comparison between experimental PDF data and simulated models for sp^2 and sp^3 carbon reveals a peak at ~2.46 Å corresponding to sp^2 C–C bonds and an additional peak at ~1.54 Å indicative of sp^3 bonding, confirming a mixed hybridization state within the structure. This variation in the local atomic environment, influenced by the choice of the capping agent, directly impacts the electronic properties of the catalyst support, thereby affecting catalytic performance.[28]

Additionally, the electronic interactions between carbon atoms in the capping agents and the AuPdRuRhPt HEA nanoparticles were investigated using XPS for the analysis of C, Au, Pd, Ru, Rh, and Pt elements (Fig. 4). All the peaks were calibrated to the C 1s peak at 284.8 eV, corresponding to the C–C bond. XPS survey spectra of both HEA variants were recorded in the range of 0–1200 eV (Fig. S6). The Au 4f peaks were observed at 84.2 eV (Au^0 $4f_{7/2}$) and 87.9 eV (Au^0 $4f_{5/2}$), indicating the presence of metallic gold. The metallic palladium (Pd^0 $3d_{5/2}$ and Pd^0 $3d_{3/2}$) peaks were located at 335.8 eV and 341.1 eV, respectively. Fig. 4(c) shows the resolved peak in the Ru 3d and C 1s regions, with BEs of 281.4 eV and 284.8 eV, which are attributed to RuO_2 and C–C. In the Rh 3d and Pt 4f regions, peaks corresponding to metallic rhodium and platinum were observed at 307.7 eV and 71.6 eV, respectively.

We also analyzed the elemental compositions of the PEG- and PVP-capped HEA NPs through both XRF and XPS analyses (Tables S1 and S2). XRF results showed similar elemental
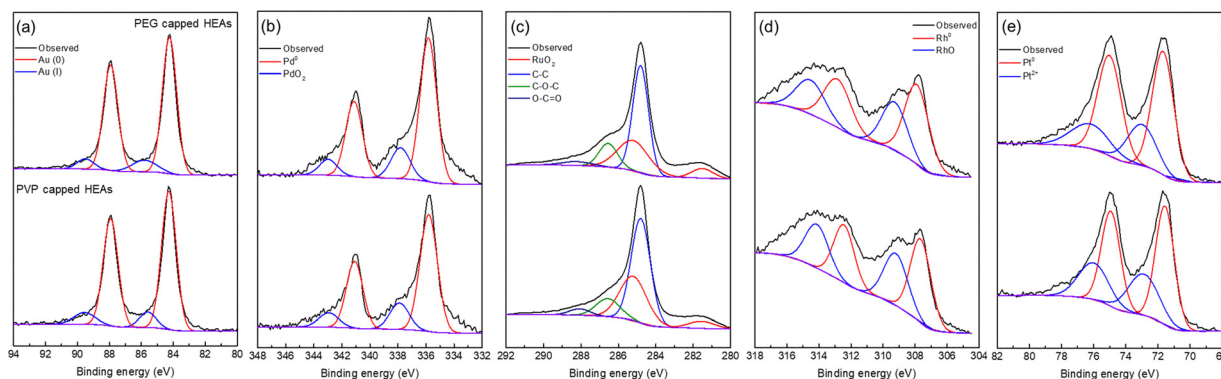
Fig. 4 High-resolution XPS spectra of (a) Au 4f, (b) Pd 3d, (c), C 1s, (d) Rh 3d, and (e) Pt 4f for PEG-capped HEA NPs (top) and PVP-capped HEA NPs (bottom).

distributions for both PEG- and PVP-capped HEA NPs. XPS analysis was performed to quantify the carbon content, which was not detectable by XRF. The carbon content in PEG capped HEA NPs was found to be higher compared to PVP capped HEA NPs, suggesting a thicker capping layer in the former. This increased carbon content in the PEG system may reduce reliance on precious metals by promoting metal–carbon interactions, thereby enhancing catalytic properties. The combined insights from XPS (surface) and XRF (bulk) reveal that while the core composition remains consistent, the surface composition, and thus the catalytic interface, is modulated by the capping agents. This highlights the importance of surface engineering using capping agents to balance activity, stability, and noble metal utilization.

To further examine the role of PEG and PVP, TGA analysis (Fig. S7) was carried out under N_2 from room temperature to 600 °C at a heating rate of 10 °C min^{-1}. An initial mass loss below 200 °C corresponds to water desorption. PEG-capped HEA NPs showed a gradual mass loss between 200 and 400 °C, while PVP-capped HEA NPs exhibited a gradual loss from 200 to 350 °C, followed by a more pronounced loss between 350 and 500 °C, consistent with the reported thermal decomposition of PEG and PVP.[24,41] The limited overall mass loss in TGA indicates that HEA NPs synthesized with a small amount of capping agent are thermally stable. In contrast, HEA NPs synthesized with a 50-fold higher amount of PEG or PVP displayed substantial mass loss and noticeable decomposition in TGA (Fig. S7), indicating that excessive capping agent coverage negatively affects thermal stability.

The PEG- and PVP-capped HEA NPs were tested as catalysts for electrochemical water-splitting reactions in 0.5 M H_2SO_4, with their performance benchmarked against commercial Pt/C for the HER and IrO_2 for the OER. The onset potentials of the capped HEA variants were 70 mV vs. RHE (PEG-capped) and 80 mV vs. RHE (PVP-capped), indicating that they require a slightly higher onset potential than commercial Pt/C (55 mV vs. RHE) as observed by linear sweep voltammetry (LSV) shown in Fig. S8. In comparison, AuPdRuRhPt nanoparticles synthesized without any capping agent exhibited a higher onset potential of 107 mV vs. RHE, indicating that PEG and PVP promote uniform

particle formation, consistent with STEM–EDS observations (Fig. S4). Additionally, HEA NPs synthesized with a 50-fold higher amount of PEG or PVP showed significantly worse HER performance, with onset potentials of 80 mV vs. RHE (50× PEG-capped) and 230 mV vs. RHE (50× PVP-capped) (Fig. S8), consistent with TGA results indicating excessive polymer coverage. These results confirm that a minimal amount of capping agent is crucial for maintaining electrochemical accessibility and optimal catalytic activity. However, since LSV results are strongly influenced by catalyst loading, they may not accurately reflect the intrinsic activity of the electrocatalyst.[42] To address this uncertainty, we further evaluated the specific activity by normalizing the current to the electrochemical surface area (ECSA) (Fig. 5a and Fig. S9, S10). As a result, both PEG-capped HEA NPs (160 mV@0.02 j_{ecsa}/mA cm^{-2}) and PVP-capped HEA NPs (165 mV@0.02 j_{ecsa}/mA cm^{-2}) demonstrated greater potential than commercial Pt/C (245 mV@0.02 j_{ecsa}/ mA cm^{-2}). At higher overpotentials, both HEA systems reach high current densities, indicating efficient mass transport and abundant active sites, crucial for stable operation at industrially relevant current densities.

The PEG-capped HEA NPs show a better performance with a Tafel slope of 47.2 mV dec^{-1}, while the PVP-capped HEA NPs exhibit a slightly higher Tafel slope of 50.2 mV dec^{-1} (Fig. 5b). These values suggest a mixed reaction mechanism or potentially different rate-determining steps compared to the commercial Pt/C,[9,43] which has a lower Tafel slope of 38.2 mV dec^{-1}. The charge transfer resistance was evaluated using the Nyquist plot derived from EIS measurements, following a similar trend with PEG-capped HEA NPs having a smaller semicircle diameter than PVP-capped HEA NPs, indicating efficient electron transfer aligning with the observed catalytic performance (Fig. 5c). Turnover frequencies (TOF) normalized by ECSA show comparable HER activity for both PEG- and PVP-capped HEA NPs at potentials of −0.05, −0.1, −0.15, and −0.2 V vs. RHE (Fig. 5d). PEG-capped HEA NPs generally exhibit slightly higher intrinsic activity, with a minor reversal at −0.2 V where PVP shows a marginally higher TOF. TOF based on total metal loading (ECSA-uncorrected; Fig. S11) consistently indicates that PEG-capped HEA NPs are slightly more active. These observations suggest that, under the present conditions of using low concentrations and only PEG or
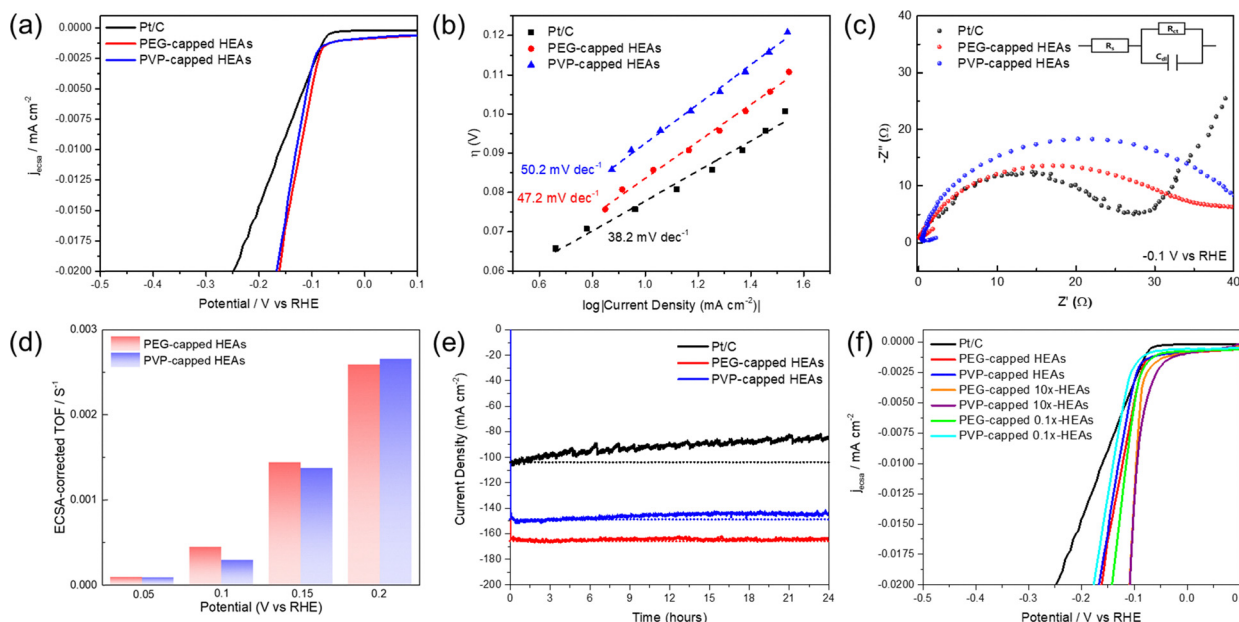
Fig. 5 Comparative electrochemical HER activity showing (a) the ECSA-normalized current density curve, (b) Tafel slope, (c) Nyquist plots of EIS, (d) calculated ECSA-corrected TOF values at different potentials for PEG- and PVP-capped HEA NPs, (e) chronoamperometry curve, and (f) ECSA-normalized current density curve with different HEA loading samples.

PVP capping agents with nanometer-sized particles, particle size and ligand variations have minimal impact on intrinsic activity per accessible site. In addition, HEA nanoparticles synthesized without capping agents show very low ECSA and unstable morphology, and therefore only geometric TOF values are reported (Fig. S11).

To test the stability of the HEA variants with the commercial Pt/C catalyst, a 24-hour chronoamperometry experiment was performed in 0.5 M H_2SO_4 at -0.2 V *vs.* RHE (Fig. 5e). The PEG-capped HEA NPs maintained the highest current density ($\sim$168 mA cm^{-2}, 99.4%) with minimal degradation followed by the PVP-capped HEA NPs ($\sim$145 mA cm^{-2}, 98.6%), whereas Pt/C showed a significantly lower current density ($\sim$100 mA cm^{-2}, 80%) with a large drop by $\sim$20 mA cm^{-2}. Furthermore, the STEM–EDS mapping of the PEG- and PVP-capped HEA NPs after the stability test (Fig. S12 and S13) confirms that the AuPdRuRhPt HEA nanoparticles retain their morphology even after prolonged HER.

To further investigate catalytic performance, we tested the effect of catalyst loading on overall current density, thereby activating more surface sites to participate in the reaction. The morphology under controlled catalyst loading conditions was confirmed by HR-TEM analysis (Fig. S14), which revealed some aggregation while maintaining a particle size distribution of 2–10 nm. The intrinsic catalytic activity for the HER was compared by varying the mass loading of HEA NPs by a factor of 10× as shown in Fig. 5f and Table S3. As a result, when the catalyst loading was increased by a factor of 10×, the PEG-capped HEA NPs showed a 1.47-fold increase in overpotential relative to the standard 1× loading. This demonstrates that controlling the overall current density by adjusting catalyst loading can effectively regulate HER performance.[26]

Since the HEA NPs composed of elements that are known to be active for the OER, we assessed their performance for the OER under the same electrochemical conditions, as presented in Fig. S15. Both the electrochemical activity and 24-hour chronopotentiometric stability tests showed that the PEG-capped HEA NPs exhibited the highest performance, followed by the PVP-capped HEA NPs then commercial IrO$_2$. The Tafel slopes for the PEG- and PVP-capped HEA NPs were calculated to be 120 mV dec^{-1} and 125.1 mV dec^{-1}, respectively, substantiating that the smaller particle size from PEG capping likely leads to a greater number of exposed active sites. Overall, despite the significant structural differences clearly observed through TEM, PDF, and XPS analyses, the performance gap between the two HEA variants remained relatively modest. This suggests that the multi-metallic composition with capping agents likely helps stabilize the electronic properties, thereby reducing the impact of morphological variations.

Conclusion

This work presents a simple yet effective strategy to overcome a key challenge in the synthesis of the AuPdRuRhPt high entropy alloy (HEA), which is aggregation of ultra-small HEA nanoparticles. By employing PEG and PVP capping agents *via* a wet-chemical approach, aggregation was suppressed while particle size and atomic arrangement were controlled, as revealed by synchrotron-based WAXS, PDF, HR-TEM, and XPS analyses. These structural differences directly correlate with variations in electrochemical performance, particularly in HER and OER activities, demonstrating the importance of structural factors in optimizing catalytic performance. The PEG-capped HEA NPs exhibited superior catalytic performance, requiring lower overpotentials of 87 mV

for the HER and 270 mV for the OER, compared to commercial Pt/C and IrO₂. Overall, this work establishes a viable method for stabilizing ultrasmall HEA catalysts and highlights the importance of interface control in optimizing catalytic function. The findings open new directions for the rational design of HEA catalysts where surface structure, electronic states, and support interactions can be systematically tuned. Future investigations should explore the dynamic evolution of these nanostructures under operating conditions and on extending the capping-agent strategy to other alloy systems and electrochemical reactions.

Author contributions

S. J. conceptualized the study, carried out the data collection and analysis, and wrote the manuscript. S. W. B. and P. N. collected the data and wrote the manuscript. M. B. R. designed the systems, analyzed the data, and wrote the manuscript. All authors commented on the manuscript.

Conflicts of interest

The authors declare no competing interests.

Data availability

The data supporting this article have been included as part of the supplementary information (SI). Supplementary information: original HR-TEM and STEM-EDS mapping data, PDF gui-simulation models, XPS, TGA, electrochemical measurements (LSV, CV, EIS, TOF, OER activity), and XRF data. See DOI: https://doi.org/10.1039/d5nh00631g.

Acknowledgements

References

1 S. Chu and A. Majumdar, *Nature*, 2012, **488**, 294–303.
2 K. Kodama, T. Nagai, A. Kuwaki, R. Jinnouchi and Y. Morimoto, *Nat. Nanotechnol.*, 2021, **16**, 140–147.
3 Z. Zhao, C. Chen, Z. Liu, J. Huang, M. Wu, H. Liu, Y. Li and Y. Huang, *Adv. Mater.*, 2019, **31**, 1808115.
4 Z. P. Ifkovits, J. M. Evans, M. C. Meier, K. M. Papadantonakis and N. S. Lewis, *Energy Environ. Sci.*, 2021, **14**, 4740–4759.
5 Y. Lin, Y. Dong, X. Wang and L. Chen, *Adv. Mater.*, 2023, **35**, 1–38.
6 Y. Zhou, W. Guo, L. Xing, Z. Dong, Y. Yang, L. Du, X. Xie and S. Ye, *ACS Cent. Sci.*, 2024, **10**, 2006–2015.
7 M. Luo and M. T. M. Koper, *Nat. Catal.*, 2022, **5**, 615–623.
8 A. Lončar, D. Escalera-López, S. Cherevko and N. Hodnik, *Angew. Chem., Int. Ed.*, 2022, **61**, e202114437.
9 X. Zou and Y. Zhang, *Chem. Soc. Rev.*, 2015, **44**, 5148–5180.
10 Z. X. Cai, H. Goou, Y. Ito, T. Tokunaga, M. Miyauchi, H. Abe and T. Fujita, *Chem. Sci.*, 2021, **12**, 11306–11315.
11 Y. Sun and S. Dai, *Sci. Adv.*, 2021, **7**, 1–23.
12 M. Fu, X. Ma, K. Zhao, X. Li and D. Su, *iScience*, 2021, **24**, 102177.
13 J.-W. Yeh, S.-K. Chen, S.-J. Lin, J.-Y. Gan, T.-S. Chin, T.-T. Shun, C.-H. Tsau and S.-Y. Chang, *Adv. Eng. Mater.*, 2004, **6**, 299–303.
14 H. Li, J. Lai, Z. Li and L. Wang, *Adv. Funct. Mater.*, 2021, **31**, 2106715.
15 D. B. Miracle and O. N. Senkov, *Acta Mater.*, 2017, **122**, 448–511.
16 M. Li, F. Lin, S. Zhang, R. Zhao, L. Tao, L. Li, J. Li, L. Zeng, M. Luo and S. Guo, *Sci. Adv.*, 2024, **10**, 1–21.
17 H. Cai, H. Yang, S. He, D. Wan, Y. Kong, D. Li, X. Jiang, X. Zhang, Q. Hu and C. He, *Angew. Chem., Int. Ed.*, 2025, **64**, e202423765.
18 S. Feng, X. Song, Y. Liu, X. Lin, L. Yan, S. Liu, W. Dong, X. Yang, Z. Jiang and Y. Ding, *Nat. Commun.*, 2019, **10**, 1–9.
19 K. M. Koczkur, S. Mourdikoudis, L. Polavarapu and S. E. Skrabalak, *Dalton Trans.*, 2015, **44**, 17883–17905.
20 T. M. R. Wayman, V. Lomonosov and E. Ringe, *J. Phys. Chem. C*, 2024, **128**, 4666–4676.
21 P. Savchenko, D. Zelikovich, H. Elgavi Sinai, R. Baer and D. Mandler, *J. Am. Chem. Soc.*, 2024, **146**, 22208–22219.
22 C. Fernández-López, C. Mateo-Mateo, R. A. Álvarez-Puebla, J. Pérez-Juste, I. Pastoriza-Santos and L. M. Liz-Marzán, *Langmuir*, 2009, **25**, 13894–13899.
23 H. S. Toh, K. Jurkschat and R. G. Compton, *Chem. – Eur. J.*, 2015, **21**, 2998–3004.
24 Zulfiqar, S. Afzal, R. Khan, T. Zeb, M. ur Rahman, Burhanullah, S. Ali, G. Khan, Z. ur Rahman and A. Hussain, *J. Mater. Sci.: Mater. Electron.*, 2018, **29**, 20040–20050.
25 A. Sharma and A. L. Hector, *Faraday Discuss.*, 2025, DOI: 10.1039/d5fd00088b.
26 D. Wu, K. Kusada, T. Yamamoto, T. Toriyama, S. Matsumura, S. Kawaguchi, Y. Kubota and H. Kitagawa, *J. Am. Chem. Soc.*, 2020, **142**, 13833–13838.
27 M. Luo, Y. Hong, W. Yao, C. Huang, Q. Xu and Q. Wu, *J. Mater. Chem. A*, 2015, **3**, 2770–2775.
28 G. R. Dey, C. R. McCormick, S. S. Soliman, A. J. Darling and R. E. Schaak, *ACS Nano*, 2023, **17**, 5943–5955.
29 L. Sun, K. Wen, G. Li, X. Zhang, X. Zeng, B. Johannessen and S. Zhang, *ACS Mater. Au*, 2024, **4**, 547–556.
30 S. Jeong, A. J. Branco, S. W. Bollen, C. S. Sullivan and M. B. Ross, *Nanoscale*, 2024, **16**, 11530–11537.
31 C. Li and J. B. Baek, *ACS Omega*, 2020, **5**, 31–40.
32 D. Wu, K. Kusada, T. Yamamoto, T. Toriyama, S. Matsumura, I. Gueye, O. Seo, J. Kim, S. Hiroi, O. Sakata, S. Kawaguchi, Y. Kubota and H. Kitagawa, *Chem. Sci.*, 2020, **11**, 12731–12736.
33 Materials Project Team, The Materials Project, https://next-gen.materialsproject.org/materials.

34 C. L. Farrow, P. Juhas, J. W. Liu, D. Bryndin, E. S. Boin, J. Bloch, T. Proffen and S. J. L. Billinge, *J. Phys.: Condens. Matter*, 2007, **19**, 335219.

35 Y. Yao, Q. Dong, A. Brozena, J. Luo, J. Miao, M. Chi, C. Wang, I. G. Kevrekidis, Z. J. Ren, J. Greeley, G. Wang, A. Anapolsky and L. Hu, *Science*, 2022, **376**, 3103.

36 Y. Yao, Z. Huang, P. Xie, S. D. Lacey, R. J. Jacob, H. Xie, F. Chen, A. Nie, T. Pu, M. Rehwoldt, D. Yu, M. R. Zachariah, C. Wang, R. Shahbazian-Yassar, J. Li and L. Hu, *Science*, 2018, **359**, 1489–1494.

37 I. A. Safo, C. Dosche and M. Özaslan, *Chem. Phys. Chem.*, 2019, **20**, 3010–3023.

38 M. Tejamaya, I. Römer, R. C. Merrifield and J. R. Lead, *Environ. Sci. Technol.*, 2012, **46**, 7011–7017.

39 R. Javed, M. Usman, S. Tabassum and M. Zia, *Appl. Surf. Sci.*, 2016, **386**, 319–326.

40 B. Ajitha, Y. A. Kumar Reddy, P. S. Reddy, H. J. Jeon and C. W. Ahn, *RSC Adv.*, 2016, **6**, 36171–36179.

41 R. Li, Y. Wu, Z. Bai, J. Guo and X. Chen, *RSC Adv.*, 2020, **10**, 42120–42127.

42 S. Anantharaj and S. Kundu, *ACS Energy Lett.*, 2019, **4**, 1260–1264.

43 C. G. Morales-Guio, L. A. Stern and X. Hu, *Chem. Soc. Rev.*, 2014, **43**, 6555–6569.